Relativistic quantum scarring, spin-induced phase, and quantization in a symmetric Dirac billiard system

Zi-Yuan Li[1,2], Li-Li Ye[1,3], Rui-Hua Ni[1], Cheng-Zhen Wang[4], Liang Huang[1], Ying-Cheng Lai[3,5] and Celso Grebogi[6]

[1] Lanzhou Center for Theoretical Physics and Key Laboratory for Magnetism and Magnetic Materials of the Ministry of Education, Lanzhou University, Lanzhou, Gansu 730000, China

[2] The Greater Bay Area Branch of Aerospace Information Research Institute, Chinese Academy of Sciences, Guangzhou 510535, China

[3] School of Electrical, Computer and Energy Engineering, Arizona State University, Tempe, Arizona 85287, USA

[4] Wave Transport in Complex Systems Lab, Physics Department, Wesleyan University, Middletown, Connecticut 06459, USA

[5] Department of Physics, Arizona State University, Tempe, Arizona 85287, USA

[6] Institute for Complex Systems and Mathematical Biology, King's College, University of Aberdeen, Aberdeen AB24 3UE, United Kingdom

27 June 2022

Abstract. Thirty-five years ago, Sir Michael Berry and his collaborator Mondragon studied the behaviors of neutrino, a massless relativistic quantum particle, in a classically chaotic billiard - the neutrino billiard problem. To celebrate Sir Michael Berry's eightieth birthday, here we report results on the role of geometric symmetries of the billiard system in relativistic quantum scarring. In particular, we investigate a Dirac billiard system with a four-fold rotational symmetry whose classical dynamics are fully chaotic. The system is described by the massless Dirac equation in the fundamental domain that consists of one fourth of the full billiard, with proper boundary conditions on the symmetry lines to preserve the physical properties under the symmetry operations. We show that the relativistic quantum characteristics of spin induced phase play a fundamental role in the quantum behaviors of the Dirac particle in the billiard. We find that the peaks in the length spectra are due to the interference of states circling the fundamental domain orbits (FDOs) in opposite propagating directions, which can be constructive or destructive depending on the accumulated phases. In addition, we derive the quantization conditions of the scarring states about the unstable periodic orbits within the fundamental domain from the phase along the FDOs. Our work is a vivid demonstration that relativistic quantum scarring, or more generally quantum manifestations of classical chaos, can be fully understood by analyzing the behaviors of the geometric phase - a powerful approach in modern physics pioneered by Sir Michael Berry.

1. Introduction

Sir Michael Berry is a pioneer and one of the most influential academics in the field of Quantum Chaos. In classical systems, the hallmark of chaos is sensitive dependence on initial conditions and a necessary condition for the sensitivity to arise is that the system be nonlinear. However, in quantum systems, the fundamental Schrödinger or Dirac equations are linear. As a result, in general a sensitive dependence on initial conditions cannot occur in quantum systems, so "real" chaos cannot arise in quantum systems. Longer than three decades since, Sir Michael Berry incisively stated [1]: "There is no quantum chaos, in the sense of exponential sensitivity to initial conditions, but there are several novel quantum phenomena which reflect the presence of classical chaos. The study of these phenomena is *quantum chaology*." Nevertheless, the somewhat misleading term "Quantum Chaos" has survived. It is now agreed among most physicists that the field of quantum chaos means the study of the manifestations or fingerprints of classical chaos in quantum systems [2, 3]. Traditional quantum chaos deals with nonrelativistic quantum systems described by the Schrödinger equation, whose characteristic feature is a quadratic dependence of the energy on the momentum [4, 5, 6, 7, 8, 9, 10, 11, 12]. The relatively more recent field of relativistic quantum chaos [13, 14, 15] deals with relativistic quantum systems described by the Dirac equations with a linear energy-momentum relation.

The ground-breaking work on relativistic quantum manifestations of classical chaos was due to Sir Michael Berry and his collaborator Mondragon, in which the quantum behaviors of a neutrino in a classically chaotic billiard were studied - the so-called neutrino billiard [13]. The system is described by the massless Dirac equation for spin-1/2 particles, subject to hard-wall boundaries mathematically described by the infinite-mass confinement, where the time-reversal symmetry is broken in the absence of any magnetic field. It was shown that for the chaotic Africa neutrino billiard, a cubic conformal map of the unit circle, the eigenvalues are locally distributed according to the statistics of the Gaussian unitary ensemble in the random matrix theory. About ten years ago, a uniquely relativistic quantum class of scarring states in such billiard was discovered, which are chiral scars about selective classical periodic orbits with an odd number of reflections at the boundary [16]. For a chiral scar, due to the time reversal symmetry breaking, the counterclockwise and the clockwise propagations along the underlying classical periodic orbits are nonequivalent [16]. Later, it was found that the chiral scars can be tuned by a vertical magnetic flux through the billiard domain [17]. Quite recently, a framework unifying the traditional scars in nonrelativistic quantum systems [18, 19] and the relativistic quantum scars was established through the solutions of the massive Dirac equation in chaotic billiards with the particle mass being a tunable parameter [20].

Systematic research in relativistic quantum chaos was motivated by the tremendous development of Dirac materials [21, 22] in the past two decades. The most commonly studied Dirac material is graphene [23, 24, 25], an atomic layer of the hexagonal lattice

form of carbon. Starting with graphene, a variety of two-dimensional (2D) solid state materials have been discovered, in which the low energy excitations (quasiparticles) exhibit a linear dependence of the energy on the momentum. Such a linear dispersion relation is characteristic of classical relativistic particles, e.g., a photon or a neutrino. As a result, it is necessary to use the Dirac equation to describe the physics of the 2D Dirac materials. The field of relativistic quantum chaos seeks to uncover, understand, and exploit fundamental phenomena arising from the interplay of chaos with relativistic quantum mechanics [14, 15, 26]. In terms of fundamental science, the field connects the three revolutionary concepts of modern physics: relativity, quantum mechanics, and chaos theory. From an applied perspective, the field has the potential to lead to new methodologies in developing next generation's nanoscale electronics and spintronics based on Dirac materials.

In the original neutrino-billiard work [13], the billiard domain possesses no geometric symmetry. Here, to honour Sir Michael Berry's eightieth birthday, we extend the study to billiard systems with a geometric symmetry and focus on the new physical phenomena arising from the interplay among the symmetry, chaos, and relativistic quantum mechanics. To be concrete, we investigate a two-dimensional (2D) relativistic massless Dirac billiard with a four-fold rotational symmetry. The entire billiard domain can be divided into four fundamental domains, and any periodic orbit can be decomposed into the fundamental domain orbits (FDOs), each residing in one fundamental domain [27]. Unlike nonrelativistic quantum billiards described by the Schrödinger equation in which the time reversal symmetry is preserved, there is time-reversal symmetry breaking not only in the whole billiard domain but also in each symmetric subdomain. By calculating and analyzing the peaks of the length spectra located at different periodic orbits, we find that the breaking of the time reversal symmetry in the fundamental symmetric domain affects the spectral statistics in a nontrivial way. Specifically, due to the phase change induced by spin when the direction of particle motion is altered, e.g., associated with a reflection at the boundary, the Dirac billiard system can exhibit more complicated interference patterns in the length spectra. We derive the quantization conditions for scarring states about distinct FDOs and validate the conditions through the statistics of the scarring states in the fundamental domain. Our work is further proof that the principle of geometric phase, a powerful approach in modern physics pioneered by Sir Michael Berry, can be used to understand the intricate behaviors arising from the interplay among symmetry, chaos, and relativistic quantum mechanics.

2. Symmetries, Dirac Hamiltonian, conformal mapping method, and basic solution properties

2.1. Exploiting symmetries in quantum chaotic billiards

When a quantum system possesses certain discrete symmetries, the physical properties of the fundamental domain may differ from those of the original system [28, 29, 30, 31]. For example, if a system has the time-reversal symmetry and a three-fold rotational symmetry, a subsystem determined by the rotational symmetry group may violate the time-reversal symmetry and such a violation has signatures in, e.g., the energy level-spacing statistics [28]. It has been well established that the quantum spectral statistics of classically chaotic systems follow universal classes as determined by the random-matrix theory [32, 33, 34, 35, 36, 2, 37, 3, 38]. In particular, if a system preserves the time reversal symmetry but no other discrete symmetries, the energy level-spacing statistics follow the class of Gaussian orthogonal ensembles (GOE). When the time reversal symmetry is broken, the spectral statistics belong to the class of Gaussian unitary ensembles (GUE). If the classical dynamics are integrable, the spectra follow the Poisson statistics [39]. The GOE statistics in systems with the time-reversal symmetry and the GUE statistics in situations where this symmetry is broken were previously confirmed in microwave billiard experiments [40, 41, 42, 43, 29, 30, 31].

The classical dynamics of a billiard system with discrete symmetries can be conveniently studied through its fundamental domains, where the whole system can be constructed through symmetric operations such as duplication, reflection, rotation, and attachment along the symmetry lines between two adjacent fundamental domains. Accordingly, any original periodic orbit can be decomposed into FDOs residing only in a fundamental domain [27]. For the corresponding quantum system, the Hamiltonian of the whole system has a block form determined by the discrete symmetry, where each block represents a symmetric subspace. The study of the quantum behaviors of the whole system can often be greatly facilitated by focusing on the subsystem in a fundamental domain and applying proper connecting conditions at the symmetry lines separating the fundamental domains. There is complete equivalence between the properties under the symmetry operation for the subsystem and those of the original system. Previously, a semiclassical analysis of quantum billiards with discrete symmetries was developed, unraveling the role played by the FDOs in the spectral fluctuation properties [44, 45, 46, 47].

Quite recently, a Schrödinger billiard with a four-fold rotational symmetry was studied [48], where it was observed that intriguing interference patterns can arise in the length spectra. In comparison with a billiard system with a threefold symmetry [49], the four-fold symmetric system has the advantage that the interference due to the FDOs can be maximally enhanced or destroyed.

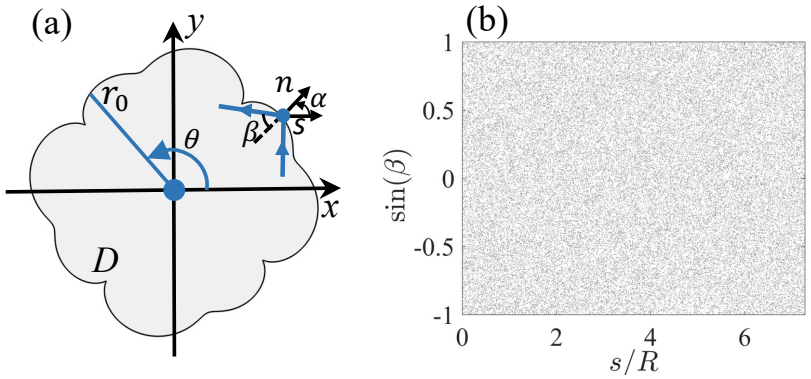

Figure 1. Billiard system with the four-fold rotational symmetry. (a) A sketch of the two-dimensional billiard domain D with boundary (r, θ) determined by Eq. (5), where α is the angle from the positive x axis to the normal direction $\boldsymbol{n}$ at arc length s. θ and s are counted from positive x axis. There is no mirror reflection symmetry in the system. (b) The Poincare surface of section for the ray dynamics in the billiard, indicating fully chaotic motion.

2.2. Relativistic quantum (Dirac) billiard with four-fold rotational symmetry

A relativistic massless spin-half particle confined in a finite 2D domain D by an infinite mass boundary [13], as shown in Fig. 1, is described by the following Hamiltonian:

$$\hat{H} = -i\hbar v_F \hat{\boldsymbol{\sigma}} \cdot \nabla + V(\boldsymbol{r})\sigma_z, \tag{1}$$

where v_F is the Fermi velocity, $\hat{\boldsymbol{\sigma}} = (\sigma_x, \sigma_y)$ and σ_z are Pauli matrices, the potential $V(\boldsymbol{r})$ is zero inside D and infinite outside. The corresponding free-space eigenvalue problem is

$$-i \begin{pmatrix} 0 & \partial_x - i\partial_y \\ \partial_x + i\partial_y & 0 \end{pmatrix} \begin{pmatrix} \psi_1(\boldsymbol{r}) \\ \psi_2(\boldsymbol{r}) \end{pmatrix} = k \begin{pmatrix} \psi_1(\boldsymbol{r}) \\ \psi_2(\boldsymbol{r}) \end{pmatrix}, \tag{2}$$

where k is the wavevector with the energy $E = \hbar v_F k$, and $\psi(\boldsymbol{r}) = [\psi_1(\boldsymbol{r}), \psi_2(\boldsymbol{r})]^T$ is the two-component spinor wavefunction subject to the hard-wall type of boundary conditions. The infinite mass potential outside the domain boundary causes the local current in the normal direction of the boundary to vanish: $\boldsymbol{j} \cdot \boldsymbol{n} = 0$, with the relativistic current $\boldsymbol{j}$ defined as

$$\boldsymbol{j}(\boldsymbol{r}) = v_F \psi^\dagger \hat{\boldsymbol{\sigma}} \psi = 2v_F[\Re(\psi_1^* \psi_2), \Im(\psi_1^* \psi_2)]. \tag{3}$$

The corresponding boundary condition for the spinor wavefunction can be conveniently written as [13]

$$\left. \frac{\psi_2(\boldsymbol{r}_0)}{\psi_1(\boldsymbol{r}_0)} \right|_{\boldsymbol{r}_0 \in \partial D} = i \exp(i\alpha), \tag{4}$$

where ∂D is the boundary of domain D and α is the angle from the positive x axis to the normal direction of the boundary in the counterclockwise direction, as shown in Fig. 1(a).

The domain of the billiard has a four-fold rotational symmetry, which can be mapped from the unit disk in the complex plane by the following complex function [48]

$$w = [z(1 + 0.075z^4 + 0.075e^{i\frac{\pi}{2}}z^8)] \times R, \tag{5}$$

with R defining the scale of the system and z belongs to the unit disk

$$z = \rho \exp(i\phi), \quad \phi \in [0, 2\pi] \text{ and } \rho \in [0, 1], \tag{6}$$

where $\rho = 1$ yields the boundary points $\boldsymbol{r}_0 \in \partial D$. The position vector $\boldsymbol{r} \in D$ can be expressed in the Cartesian coordinates as $[x, y] = [\Re(w(z)), \Im(w(z))]$, or in the polar coordinates as (r, θ) with $r = \text{abs}(w)$ and $\theta = \arg(w)$. It is straightforward to verify $r_0(\theta + \pi/2) = r_0(\theta)$. The fundamental domain can be chosen as the region enclosed by the radial lines $\theta = \theta_0$ and $\theta = \theta_0 + \pi/2$ for any θ_0 with r running from 0 to r_0. The classical ray dynamics of this billiard is fully chaotic, as shown in Fig. 1(b), with the largest Lyapunov exponent being about 0.935 [48].

The four-fold rotationally symmetric Dirac billiard system is invariant under rotation $\hat{\mathcal{R}}$ of $\pi/2$:

$$\hat{\mathcal{R}} = e^{-\frac{i}{\hbar}\frac{\pi}{2}\hat{J}_z} = e^{-\frac{i}{\hbar}\frac{\pi}{2}(\hat{L}_z + \hat{s}_z)},$$

where $\hat{L}_z = -i\hbar\frac{\partial}{\partial\theta}$ is the angular momentum operator about the z axis, $\hat{s}_z = (\hbar/2)\sigma_z$ is the spin operator in the z direction, and $\hat{J}_z = \hat{L}_z + \hat{s}_z$ is the total angular momentum operator about the z axis, which commutes with the Hamiltonian $[\hat{H}, \hat{\mathcal{R}}] = 0$. The eigenwavefunctions of $\hat{H}$ can then be chosen to be the eigenwavefunctions of $\hat{\mathcal{R}}$:

$$\hat{\mathcal{R}}\psi^{(m)}(r, \theta) = e^{-i\frac{\pi}{2}(m+\frac{1}{2})}\psi^{(m)}(r, \theta)$$

for $m = 0, 1, 2, 3$ as the value only depends on mod(m,4). Another useful property is

$$\hat{\mathcal{R}}\psi^{(m)}(r, \theta) = \psi'^{(m)}(r, \theta) = e^{-\frac{i}{2}\frac{\pi}{2}\sigma_z}\psi^{(m)}(r, \theta - \frac{\pi}{2}),$$

where $\psi'^{(m)}(r, \theta)$ is the wavefunction obtained after rotating $\psi^{(m)}(r, \theta)$ by $\hat{\mathcal{R}}$ and the second equality is the property of the two-component spinor wavefunction which can be verified from the wavefunctions in a system with rotational symmetry, e.g., a circular confinement. We thus have

$$\psi^{(m)}(r, \theta + \frac{\pi}{2}) = \begin{pmatrix} e^{im\frac{\pi}{2}} & 0 \\ 0 & e^{i(m+1)\frac{\pi}{2}} \end{pmatrix} \psi^{(m)}(r, \theta). \tag{7}$$

The Hamiltonian evaluated on a set of base functions with the above property [e.g., Eq. (16)] can be written in a diagonalized form:

$$H = \begin{pmatrix} H^{(0)} & & & \\ & H^{(1)} & & \\ & & H^{(2)} & \\ & & & H^{(3)} \end{pmatrix}, \tag{8}$$

where each block $H^{(m)}$ $(m = 0, 1, 2, 3)$ corresponds to a symmetric subspace and has its own eigenenergy and eigenwavefunctions:

$$H^{(m)}\psi_j^{(m)}(\boldsymbol{r}) = E_j^{(m)}\psi_j^{(m)}(\boldsymbol{r}). \tag{9}$$

The calculation is simplified as only each block $H^{(m)}$ needs to be diagonalized instead of the full Hamiltonian matrix [Eq. (8)]. Equivalently, the Hamiltonian (1) can be solved on a fundamental domain, $\theta \in [\theta_0, \theta_0 + \pi/2)$, to obtain $E_j^{(m)}$ and $\psi_j^{(m)}(\boldsymbol{r})$ for each m, where $\boldsymbol{r}$ is in this fundamental domain, with the boundary given by Eq. (7). In our study, the eigenenergies and eigenwavefunctions are obtained from Eq. (9), while the fundamental domain is only being used to derive the phase accumulation along the FDOs, where θ_0 is chosen accordingly in order to analyze different FDOs.

2.3. Solutions of Dirac equation in the four-fold chaotic billiard: conformal mapping method

To solve the eigenequation (2) with the boundary condition (4) in domain D in the w plane, we employ the conformal mapping method [16, 50]. Briefly, the domain D generating classical chaos can be mapped to the unit disk $z = \rho e^{i\phi}$ with $\rho \in [0, 1]$ and $\phi \in [0, 2\pi)$ through the inverse mapping of Eq. (5), where the Dirac equation can be analytically solved. In particular, in the complex $z = (\rho, \phi)$ plane, the solutions of the Dirac equation in the unit disk subject to the boundary condition (4) can be written as

$$\overline{\psi}_{l,q}(\rho, \phi) = \widetilde{N}_{l,q} \exp(il\phi) \begin{pmatrix} J_l(\mu_{l,q}\rho) \\ i\exp(i\phi)J_{l+1}(\mu_{l,q}\rho) \end{pmatrix}, \tag{10}$$

where $l = \cdots, -1, 0, 1, \cdots$, $q = 1, 2, 3, \cdots$, $J_l(\mu_{l,q}\rho)$ is the Bessel function, $\mu_{l,q}$ is the eigenvalue and it is the qth zero of $J_l(\mu_{l,q}) - J_{l+1}(\mu_{l,q})$ [Eq. (104) in Ref. [13]], and

$$\widetilde{N}_{l,q} = 1 \Big/ \sqrt{2\pi \int_0^1 \mathrm{d}\rho\rho[J_l^2(\mu_{l,q}\rho) + J_{l+1}^2(\mu_{l,q}\rho)]}$$

is the normalization constant.

In the original complex w plane, we apply the differential operator twice to Eq. (2) to get

$$-\nabla^2\psi(\boldsymbol{r}) = k^2\psi(\boldsymbol{r}). \tag{11}$$

Since the function $w(z)$ is analytic, we replace the ∇^2 by $\nabla_z^2/|\mathrm{d}w/\mathrm{d}z|^2$ in Eq. (11), where $\psi(\boldsymbol{r}) = e^{-i\frac{\theta_{\mathrm{cm}}}{2}\sigma_z}\psi(z) \approx \psi(z)$ with $\theta_{\mathrm{cm}} = \arg(\mathrm{d}w/\mathrm{d}z)$ being the angle induced by the rotation of the spinor wavefunction due to the conformal mapping. With this change of variable, in the unit disk of the complex z plane, Eq. (11) becomes

$$-\frac{1}{|\mathrm{d}w/\mathrm{d}z|^2}\nabla_z^2\psi(z) = k^2\psi(z). \tag{12}$$

Due to the functional form of the conformal mapping (5), the operator $-\frac{1}{|\mathrm{d}w/\mathrm{d}z|^2}\nabla_z^2$ has the four-fold rotational symmetry too. The analytic solution set of the Dirac equation,

$\{\overline{\psi}_{l,q}\}$, forms an orthonormal basis satisfying the boundary condition (4) on the unit disk $|z| = \rho \leq 1$. The solution $\psi(z)$ of Eq. (12) can then be expanded as

$$\psi(\rho, \phi) = \sum_{l,q} c_{l,q} \overline{\psi}_{l,q}(\rho, \phi). \tag{13}$$

The task then becomes that of determining the coefficients $c_{l,q}$, for if they are determined, the eigenfunctions in the original billiard D can be obtained.

Substituting the expansion (13) back to Eq. (12) and exploiting the orthogonal relations of the base vectors, we get

$$\frac{\nu_{l,q}}{k^2} - \sum_{l',q'} M_{l,q,l',q'} \nu_{l',q'} = 0, \tag{14}$$

where $\nu_{l,q} = \mu_{l,q} c_{l,q}$ and the elements

$$\begin{aligned} M_{l,q;l',q'} =& \frac{\widetilde{N}_{l',q'} \widetilde{N}_{l,q}}{\mu_{l',q'} \mu_{l,q}} \int_0^{2\pi} \mathrm{d}\phi \exp(i(l'-l)\phi) \int_0^1 \mathrm{d}\rho \rho T(\rho, \phi) \\ & \times (J_l(\mu_{l,q}\rho) J_{l'}(\mu_{l',q'}\rho) + J_{l+1}(\mu_{l,q}\rho) J_{l'+1}(\mu_{l',q'}\rho)) \end{aligned}$$

define the matrix $\mathcal{M}$ with $T(\rho, \phi) = |\mathrm{d}w/\mathrm{d}z|^2$. Once the matrix elements $\{M_{l,q;l',q'}\}$ are obtained, we can solve the eigenproblem $\mathcal{M} \cdot \boldsymbol{\nu} = \lambda \boldsymbol{\nu}$ with a set of eigenvalues and eigenvectors $\{\lambda_n, \boldsymbol{\nu}^n\}$ $(n = 1, 2, \cdots)$. The expansion coefficients in Eq. (13) are then given by $c^n_{l,q} = \nu^n_{l,q}/\mu_{l,q}$ and the solutions of the Dirac equation in the original chaotic domain are

$$\psi_n(\rho, \phi) = \sum_{l,q} \nu^n_{l,q} \overline{\psi}_{l,q}/\mu_{l,q}, \tag{15}$$

with the eigenwavenumber given by $k_n = 1/\sqrt{\lambda_n}$. The eigenvalues k_n and the eigenwavefunctions $\psi_n(\boldsymbol{r})$ constitute the solution set of the original Dirac billiard system as defined by Eq. (2) and the boundary condition (4).

Two remarks are in order.

First, because of the relation $\psi(\boldsymbol{r}) = e^{-i\frac{\theta_{\mathrm{cm}}}{2}\sigma_z} \psi(z)$, the solution $\psi(z)$ satisfying the boundary condition for the unit disk on the z plane will not lead to a $\psi(\boldsymbol{r})$ satisfying the boundary condition for the billiard D. The resulting eigenwavenumber k_n and eigenwavefunction $\psi(\boldsymbol{r})$ are not precisely those for Eq. (2) subject to the boundary condition (4) in the original billiard domain D. However, this inaccuracy is significant but only for the first few eigenwavefunctions, as these wavefunctions usually have large values on the boundary, leading to errors in the eigenwavenumber as well. This inaccuracy diminishes for higher energy states, as the values of the wavefunctions on the boundary are negligible [50].

Second, since the non-uniform billiard system (12) has the four-fold rotational symmetry, the basis function $\overline{\psi}_{l,q}$ can also be grouped into four classes in terms of the values of l due to distinct responses to $\hat{\mathcal{R}}$ of $\pi/2$. The solutions can then be grouped by summing l selectively, depending on m, in the expansion equation (13):

$$\psi^{(m)} = \sum_{l_m,q} c_{l_m,q} \overline{\psi}_{l_m,q}, \tag{16}$$

where $l_m = 4p + m, \quad p = 0, \pm 1, \pm 2 \cdots$. For each value of m, the matrix $\mathcal{M}^{(m)}$ can be constructed in a similar way of (8), yielding the corresponding coefficients $c_{l_m,q}$ and the eigenvectors $k_n^{(m)}$ in the same symmetric subspace. The resulting eigenwavefunctions $\psi_n^{(m)}$ belong to the same class of m with the eigenvectors $k_n^{(m)}$. In actual calculations, the expansion (16) must be truncated. We choose the first 40,000 eigensolutions in increasing order of $\mu_{l_m,q}$ as the base to construct $\psi^{(m)}(\rho, \phi)$, whose first 10,000 solutions are accurate enough for further analysis [16].

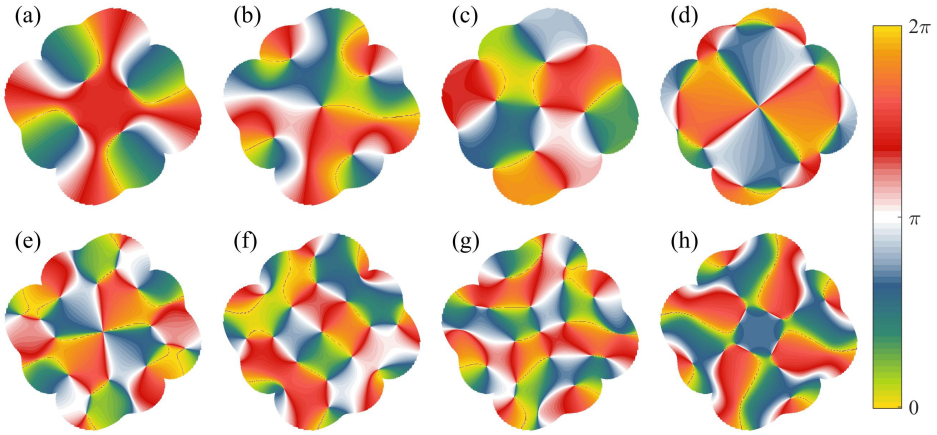

Figure 2. Phases of the spinor components belonging to different symmetry subspaces. (a,b) Phase distribution in the domain space for the first and second component of the 3rd eigenfunction of $H^{(0)}$. (c,d), (e,f) and (g,h) show the corresponding phases of the two components of the 2nd, the 5th and the 6th eigenfunction of $H^{(1)}$, $H^{(2)}$ and $H^{(3)}$, respectively.

2.4. Phase relation of the wavefunction after rotation of $\pi/2$

The phase of the spinor wavefunction plays an important role in scarring. Equation (7) stipulates that the relations of the two wavefunction components at $(r, \theta + \pi/2)$ and (r, θ) are

$$\psi_1^{(m)}(r, \theta + \frac{\pi}{2}) = \exp(im\frac{\pi}{2})\psi_1^{(m)}(r, \theta) \tag{17}$$

and

$$\psi_2^{(m)}(r, \theta + \frac{\pi}{2}) = \exp(i(m+1)\frac{\pi}{2})\psi_2^{(m)}(r, \theta), \tag{18}$$

respectively. Figure 2 shows the phase distributions of the two spinor components in space for eigenwavefunctions from $H^{(0)}$ to $H^{(3)}$. Comparing the phases of the eigenwavefunction at an arbitrary point (r, θ) and its image point after rotating $\pi/2$, $(r, \theta + \pi/2)$ through Eqs. (17) and (18), we see that the phases increase by the amounts $m\pi/2$ and $(m+1)\pi/2$ for the first and second components, respectively. We thus have that $\psi_2^{(m)}$ has the same phase relation as $\psi_1^{(m+1)}$, with $\psi_1^{(3+1)} = \psi_1^{(0)}$. For example, for $\psi_2^{(3)}$ and $\psi_1^{(0)}$, the phases at (r, θ) and $(r, \theta + \pi/2)$ are the same, as shown in Fig. 2(a,h). For $\psi_2^{(0)}$ and $\psi_1^{(1)}$, the amount of phase increment from (r, θ) to $(r, \theta + \pi/2)$ is $\pi/2$, and

the phase increase from (r, θ) to $(r, \theta + \pi)$ is π, as evidenced from Fig. 2(b,c). The same phase relation holds for other panels in Fig. 2.

2.5. Energy level-spacing statistics

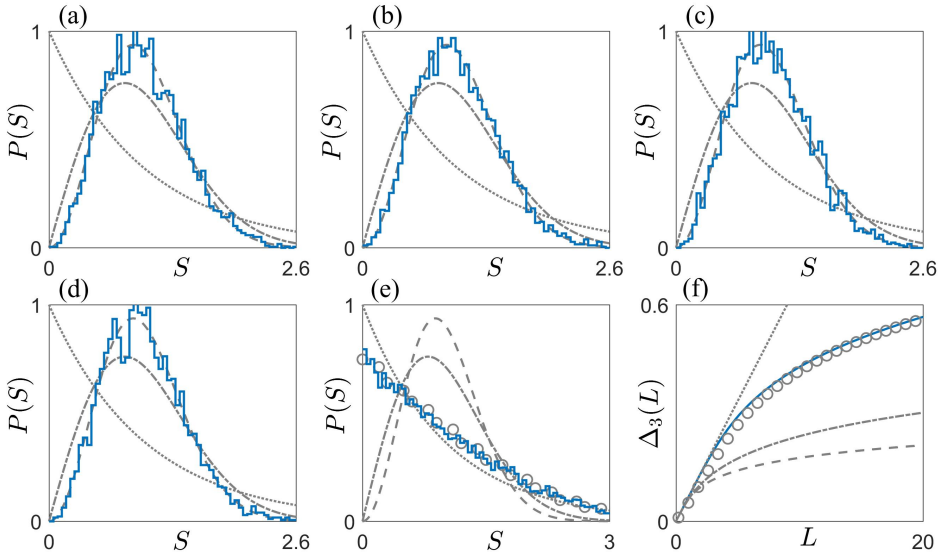

Figure 3. Level-spacing statistics. (a-d) Nearest-neighbor level spacing distributions $P(S)$ (solid staircase curves) for the symmetric subspaces $H^{(0)}, H^{(1)}, H^{(2)}$ and $H^{(3)}$, respectively. In each case, the first 3,900 eigenenergies are used for generating the statistics. (e) $P(S)$ (solid staircase curve) for the whole system with all the eigenenergies in (a-d). (f) Spectral rigidity $\Delta_3(L)$ (solid curve) for the whole system. The dotted, dash-dotted, and dashed curves are the theoretical (random-matrix) results for Poisson, GOE and GUE distributions, respectively. The circles in (e) and (f) are random matrix results with the four GUE ensembles, each with 6,000 eigenvalues.

In the Dirac Hamiltonian (1), the time reversal symmetry is broken [13]. This symmetry is broken in each block $H^{(m)}$. To compare the level-spacing statistics for different eigenenergy sets, the system-dependent details need to be removed through an unfolding procedure [15]. In particular, for a series of eigenenergies $\{E_1, E_2, \cdots, E_n, E_{n+1}, \cdots\}$, the step-wise number function $N(E)$ is the total number of eigenenergies below E. Let $\langle N(E)\rangle$ be the smooth part of $N(E)$, then $x_n \equiv \langle N(E_n)\rangle$ is the unfolded spectrum. The nearest-neighbor spacing is $S_n = x_{n+1} - x_n$ and $P(S)$ is the unfolded level-spacing statistics of the series of S_n, for which the normalization $\langle S_n\rangle = \int P(S) S \mathrm{d}S = 1$ holds regardless of the system details. In addition to $P(S)$, another important quantity characterizing the level-spacing statistics is the spectral rigidity [2] defined as

$$\Delta_3(L) = \left\langle \min(a,b) \frac{1}{L} \int_{-\frac{L}{2}}^{\frac{L}{2}} \mathrm{d}x [N(x_0 + x) - ax - b]^2 \right\rangle_{x_0}.$$

Figures 3(a)-3(d) show the distribution $P(S)$ for the unfolded spectra of $H^{(0)}$ to $H^{(3)}$, where the first 3,900 eigenenergies for each symmetric subspace are used. Figures 3(e)-3(f) show $P(S)$ and the spectral rigidity $\Delta_3(L)$ for all the eigenenergies (the solid blue curves). For the eigenfunctions from $H^{(0)}$ to $H^{(3)}$, the level spacing statistics all follow GUE, in accordance with the breaking of the time-reversal symmetry for each symmetric subspace. However, the spectral statistics for the whole system deviate from GUE. For example, while $P(S)$ is close to Poisson, the spectral rigidity $\Delta_3(L)$ is close to Poisson only when L is small - it deviates from Poisson for large L. This can be understood by noting that, since the four symmetric subspaces are uncorrelated, the level spacing statistics for the whole system resemble that of a combination of four independent eigenenergy series with each following GUE. To verify this, we generate four GUE random matrices of order 6,000, diagonalize them to yield four series of eigenvalues, and then combine them to form a single eigenvalue series. After unfolding, $P(S)$ and $\Delta_3(L)$ are plotted as circles in Figs. 3(e) and 3(f), respectively. It can be seen that they agree with the data for the whole system well.

3. Main result: length spectra and its understanding based on FDOs

Length spectra are a convenient tool to investigate the classical correspondence of quantum systems [2] as they reveal the trajectory contributions and the phase interference between conjugated orbits. The length spectra can be calculated, as follows. Once a series of eigenenergies or eigenwavenumbers are obtained, the density of states can be calculated, whose fluctuation component $\rho_{\rm osc}^{(m)}(k)$ for each symmetric subspace m can be extracted by removing the smooth component numerically.

In particular, the rotation operations $\hat{\mathcal{R}}$ of $\pi/2$ form a fourth order cyclic group $\{\hat{\mathcal{R}}^0, \hat{\mathcal{R}}^1, \hat{\mathcal{R}}^2, \hat{\mathcal{R}}^3\}$, which is Abelian, whose nonequivalent and irreducible presentations are all of dimension one. Following Ref. [44] for the symmetry-projected trace formula and Refs. [51, 52, 53, 54, 55] for analyzing the spinor wavefunction, we obtain the fluctuation component of the density of states for the mth subspace as

$$\rho_{\rm osc}^{(m)}(E) = \frac{1}{2\pi\hbar}\sum_{\gamma^{\pm}} \frac{T_{\gamma^{\pm}}}{|\det(M_{\gamma^{\pm}} - \mathbb{1}_2)|^{1/2}} \mathrm{Tr}(K_{\gamma^{\pm}}^{(m)}) \exp\left(i\frac{S_{\gamma^{\pm}}}{\hbar} - i\mu_{\gamma^{\pm}}\frac{\pi}{2}\right), \qquad (19)$$

where the summation $\gamma^{\pm}$ is over all FDOs with both forward (+) and backward (−) orientations, $T_{\gamma^{\pm}}$ denotes the primitive period of $\gamma^{\pm}$, and $M_{\gamma^{\pm}}$ is the monodromy matrix along the orbit. The trace over the spin propagator [52] $K_{\gamma^{\pm}}^{(m)}$ accounts for the effect of spin degree in the propagation of the spinor wavefunctions, the quantity $S_{\gamma^{\pm}} = \hbar k l_{\gamma}$ is the action and $\mu_{\gamma^{\pm}}$ is the Maslov index along the orbit. Note that only the spin propagator $K_{\gamma^{\pm}}^{(m)}$ depends on the orientation of the orbit and on the subspace index m. All other quantities, i.e., $T_{\gamma^{\pm}}$, $M_{\gamma^{\pm}}$, $S_{\gamma^{\pm}}$, and $\mu_{\gamma^{\pm}}$ are independent of both m and the orientation so that the notation $^{\pm}$ can be omitted for clarity. Since $E = \hbar v_F k$, $\rho_{\rm osc}^{(m)}$ can

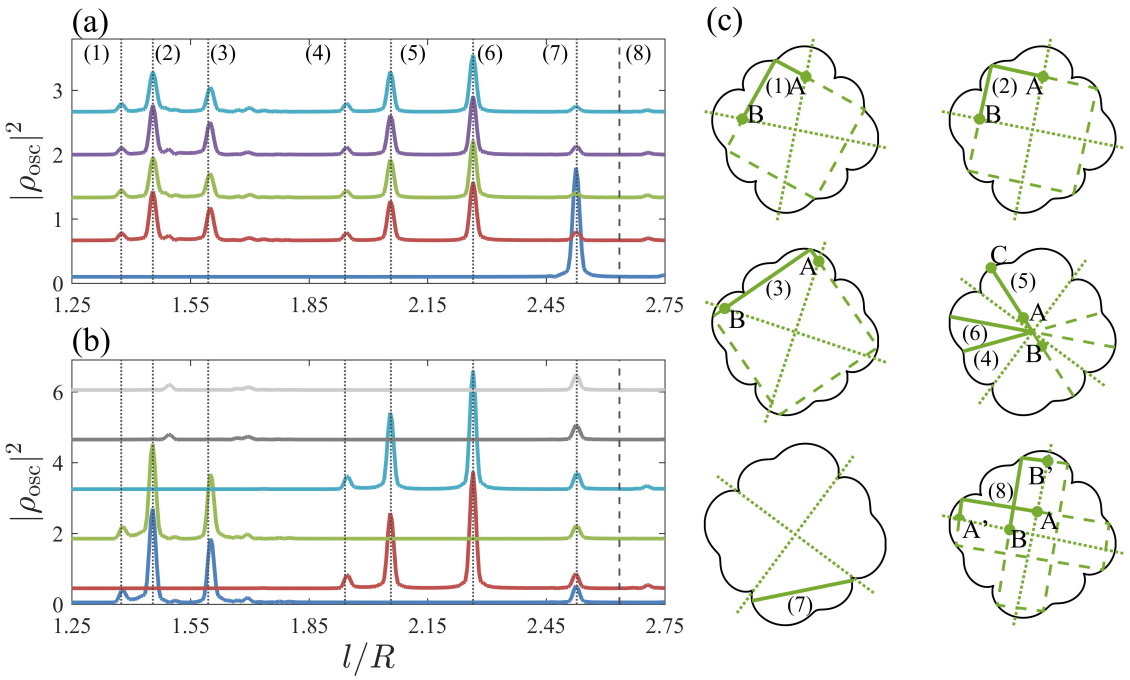

Figure 4. Length spectra in four-fold Dirac billiard. (a) From top to bottom, the length spectra for the symmetric subspaces $H^{(0)}$, $H^{(1)}$, $H^{(2)}$, $H^{(3)}$ and the spectrum for the whole system. The corresponding wavenumber k is up to $k_{\rm max} \sim 365.4/R$ and there are about 9,000 energy levels in each symmetric subspace. (b) Length spectra for different mixtures of two subspaces. From top to bottom: length spectra of the energy levels of $H^{(1,2)}$, $H^{(0,3)}$, $H^{(1,3)}$, $H^{(2,3)}$, $H^{(0,2)}$, and $H^{(0,1)}$. (c) The FDOs as represented by the solid line segments. The two dotted lines divide the whole billiard into four fundamental domains, each being a quarter of the full billiard. The numbers label the orbits corresponding to the peaks in (a). The FDOs (1-3) are one-fourth of a square. The FDOs (4-6) are one-half of a bouncing ball orbits passing through the center, leading to cross-like scarring states as a rotation by $\pi/2$ is also a solution of the system. Orbit (7) is a full bouncing ball orbit that resides completely inside a fundamental domain. The FDO (8) is one-fourth of a parallelogram orbit.

be expressed versus k

$$\rho_{\rm osc}^{(m)}(k) = \frac{v_F}{2\pi} \sum_{\gamma^\pm} \frac{T_\gamma}{|\det(M_\gamma - \mathbb{1}_2)|^{1/2}} {\rm Tr}(K_{\gamma^\pm}^{(m)}) \exp\left(i\frac{S_\gamma}{\hbar} - i\mu_\gamma \frac{\pi}{2}\right) \equiv \sum_{\gamma^\pm} A_{\gamma^\pm}^{(m)} \exp(ikl_\gamma). \tag{20}$$

The length spectra $\rho_{\rm osc}^{(m)}(l)$ can be calculated from $\rho_{\rm osc}^{(m)}(k)$ through the Fourier transform [2]:

$$\rho_{\rm osc}^{(m)}(l) = \int \rho_{\rm osc}^{(m)}(k) e^{-ikl} {\rm d}k = \sum_{\gamma^\pm} A_{\gamma^\pm}^{(m)} \delta(l - l_\gamma). \tag{21}$$

For a given subspace m and an orbit γ, $A_{\gamma^\pm}^{(m)}$ is in general different for forward and backward orbits, but the difference is typically just a phase factor:

$$A_{\gamma^+}^{(m)} = A_{\gamma^-}^{(m)} e^{i\Delta\Phi}.$$

The plot of $|\rho_{\rm osc}^{(m)}(l)|^2$ versus l exhibits peaks at lengths l_γ with the height of the peak proportional to

$$|A_{\gamma^+}^{(m)} + A_{\gamma^-}^{(m)}|^2 = |A_{\gamma^-}^{(m)}|^2 |1 + e^{i\Delta\Phi}|^2.$$

In addition, when the eigenvalues from different subspaces are mixed together, say, m_i for $i = 1, \cdots, r$ with $r < 4$, the height of the peak at l_γ will be proportional to

$$|\sum_i^r (A_{\gamma^+}^{(m_i)} + A_{\gamma^-}^{(m_i)})|^2.$$

For a true FDO that is one fourth of a full orbit, for $r = 4$, the terms cancel each other and the peaks annihilate. Therefore, it is critical to determine the relative phases of the coefficients $A_{\gamma^\pm}^{(m)}$ in order to understand the interfering behaviors of the length spectra peaks.

Numerically, there is a range for k, so the integration becomes

$$\rho_{\rm osc}^{(m)}(l) = \int_0^{k_{\rm max}} \rho_{\rm osc}^{(m)}(k) e^{-ikl} {\rm d}k, \tag{22}$$

where $k_{\rm max} \sim 365.4/R$ is the maximum wavenumber in our calculation, and there are about 9,000 energy levels in each symmetric subspace below $k_{\rm max}$.

Figure 4(a) shows the length spectra for each symmetric subspace of the four-fold Dirac billiard, where the peaks carrying the numbers from (1) to (8) correspond to the orbits within a fundamental domain shown in Fig. 4(c). We denote T as the number of reflections at the actual boundary of the whole billiard of the complete orbit, l_γ as the length of the FDOs, and L as the length of the complete orbit. The parameter values for these orbits are listed in Table 1. In Fig. 4(a), peaks (1-3) are associated with the FDOs that are one-fourth of the square-type orbits and their lengths l_γ, revealed in the spectra, are a quarter of the length L of the full orbit. Peaks (4-6) are associated with the bouncing ball orbits whose length is half of that of the full orbit, and the peak heights are identical for all the four subspaces. Because of the four-fold rotational symmetry, the corresponding scarring states are of the cross-type. Peak (7) corresponds to a bouncing ball orbit residing completely in a fundamental domain, which is a full orbit (not an FDO as in the other cases). The corresponding scarring states consist of four such orbits due to the four-fold rotational symmetry. In Fig. 4(a), the position

Table 1. Parameters of the orbits within a fundamental domain

Orbits	(1)	(2)	(3)	(4)	(5)	(6)	(7)	(8)
T	4	4	4	2	2	2	2	4
L (R)	5.5	5.815	6.405	3.895	4.113	4.529	2.528	5.269
l_γ (L)	1/4	1/4	1/4	1/2	1/2	1/2	1	1/2
l_γ (R)	1.375	1.454	1.601	1.948	2.057	2.265	2.528	2.635

of a parallelogram's FDO is also marked by (8), which is missing in the length spectra because of the destructive interference phase between motions in opposite directions.

When the energy levels from all four symmetric subspaces are combined, phase interference from the FDOs can arise. In this case, all the peaks except (7) disappear, due to the destructive interference among the FDOs, as shown by the bottom trace in Fig. 4(a). Orbit (7) is unique because, while it resides in the fundamental domain, it is a complete orbit of the original billiard without intersecting the symmetry lines defining the fundamental domains. As a result, the contributions from different symmetric subspaces are summed and squared, leading to a peak with height 16 times of that from a single subspace.

When the energy levels from two symmetric subspaces are combined, the interference becomes more complicated, and so is the resulting length spectra, as shown in Fig. 4(b). When mixing $H^{(0)}$ and $H^{(1)}$, or $H^{(2)}$ with $H^{(3)}$, peaks (1-3) are greatly enhanced but peaks (4-6) are totally annihilated. On the contrary, for the combinations of $H^{(1)}$ and $H^{(3)}$, or $H^{(0)}$ with $H^{(2)}$, peaks (1-3) are annihilated and peaks (4-6) are enhanced. For the mixture of $H^{(1)}$ and $H^{(2)}$, or $H^{(0)}$ with $H^{(3)}$, peaks (1-6) disappear. Peak (7) survives in all cases, due to its correspondence with the bouncing ball orbit within a fundamental domain.

To explain the interference patterns observed in the length spectra, we analyze the phase accumulations along the FDOs and examine the quantization conditions of the scarring states along the FDOs. That will also explain the statistics of the scarring wavefunctions on the classical orbits.

3.1. Square-type orbits (1-3)

For the scarring spinor wavefunction $\psi_j^{(m)}$ on a particular orbit in a particular symmetric subspace m, the phase accumulation around a complete cycle and thus the quantization condition can be derived, as follows. First consider the square type orbits (1-3) shown in Fig. 4(c), where the FDO contains one-fourth of the complete square orbit, with the two ends marked by A and B with $w(B) = iw(A)$. According to Eq. (7), the phase relation at the two straight symmetric lines passing through A and B points is

$$\psi_j^{(m)}\big|_B = \begin{pmatrix} e^{im\frac{\pi}{2}} & 0 \\ 0 & e^{i(m+1)\frac{\pi}{2}} \end{pmatrix} \psi_j^{(m)}\big|_A, \tag{23}$$

or

$$\psi_j^{(m)}\big|_A = \begin{pmatrix} e^{-im\frac{\pi}{2}} & 0 \\ 0 & e^{-i(m+1)\frac{\pi}{2}} \end{pmatrix} \psi_j^{(m)}\big|_B. \tag{24}$$

In the semiclassical regime, the accumulated phase for a spinor particle traveling from A to B along the FDO is contributed by two parts. The first part is from the change of the motion direction due to the reflection at the boundary, as shown in Fig. 5(a), which is

$$M_s(\Delta\theta) = \begin{pmatrix} \exp(-i\frac{\Delta\theta}{2}) & 0 \\ 0 & \exp(i\frac{\Delta\theta}{2}) \end{pmatrix}, \tag{25}$$

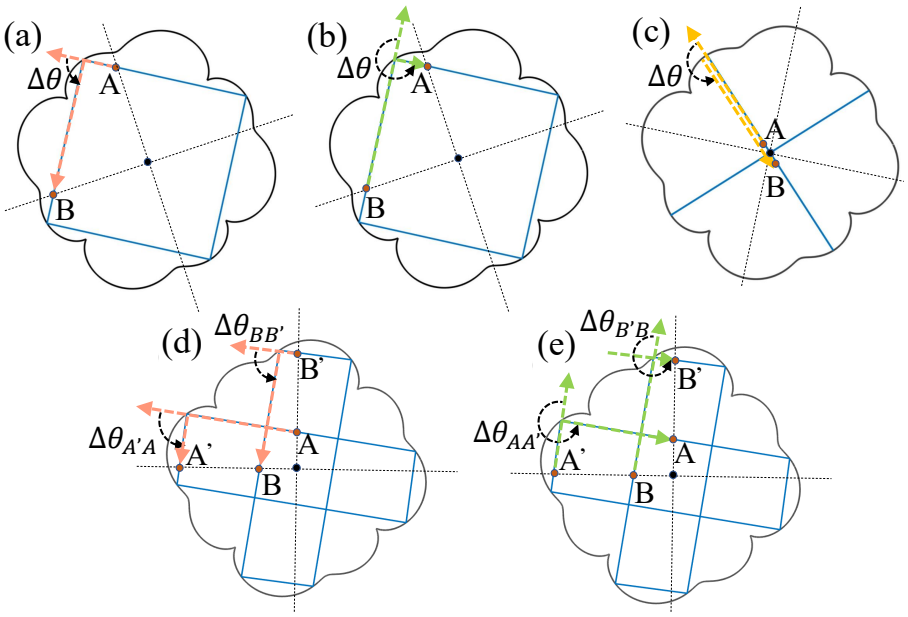

Figure 5. Angle change θ due to the reflection at the boundary for square-type orbits (1-3). The angle change for (a) the counterclockwise direction of the FDO of the square orbit within a fundamental domain as indicated by the dotted lines, (b) the clockwise direction, (c) the FDO of the bouncing ball orbit within a fundamental domain, (d) the counterclockwise direction of the FDO of the parallelogram orbit within a fundamental domain, and (e) the clockwise direction of the orbit in (d). The angle is counted counterclockwise to ensure that the reflection coefficient R is one [13, 17, 20].

where $\Delta\theta = \pi/2$ is the angle change from the motion direction before the reflection to that after the reflection, measured counterclockwise, as illustrated in Fig. 5(a). The second part is from the propagation of the spinor wave along the FDO, which is given by

$$M_{l_\gamma,\mu} = \exp\left[i(kl_\gamma - \mu\frac{\pi}{2})\right], \tag{26}$$

where k is the wavenumber, l_γ is the length of the FDO from A to B, and μ is the Maslov index. Since for the massless Dirac billiard (1), the reflection coefficient R at the infinite mass boundary equals one [13, 17, 20] (in contrast to $R = -1$ for a Schrödinger billiard with the Dirichlet boundary conditions), the reflection coefficient has no contribution to the Maslov index. Nevertheless, due to the conjugate points generated by the curved boundary along the periodic orbit, each reflection contributes one to the Maslov index. We thus have $\mu = N$, where N is the number of reflections. For this FDO of the square-type orbit, we have $N = 1$.

For a particle traveling from A to B along the FDO and then teleporting back to A via the phase relation Eq. (24), we have

$$\widetilde{\psi}_j^{(m)}\big|_A = \begin{pmatrix} e^{-im\frac{\pi}{2}} & 0 \\ 0 & e^{-i(m+1)\frac{\pi}{2}} \end{pmatrix} M_s(\frac{\pi}{2}) M_{l_\gamma,\mu}\psi_j^{(m)}\big|_A \equiv K_{\gamma^+}^{(m)} M_{l_\gamma,\mu}\psi_j^{(m)}\big|_A \equiv e^{i\Phi_+^{(m)}}\psi_j^{(m)}\big|_A,$$

where the spinor propagator

$$K_{\gamma^+}^{(m)} = \begin{pmatrix} e^{-im\frac{\pi}{2}} & 0 \\ 0 & e^{-i(m+1)\frac{\pi}{2}} \end{pmatrix} M_s(\frac{\pi}{2}) = e^{-im\frac{\pi}{2}} \begin{pmatrix} e^{-i\frac{\pi}{4}} & 0 \\ 0 & e^{-i\frac{\pi}{4}} \end{pmatrix} = e^{-im\frac{\pi}{2}-i\frac{\pi}{4}} \mathbb{1}_2$$

is reduced from an SU(2)-matrix to a U(1)-phase [53], leading to

$$\mathrm{Tr}(K_{\gamma^+}^{(m)}) = 2e^{-i\frac{\pi}{4}}.$$

Note that the phase factor $e^{-im\frac{\pi}{2}}$ is due both to the four-fold rotational symmetry and the orbital angular momentum: it is not exactly related with spin but is included here to simplify the analysis. We thus have

$$\Phi_+^{(m)} = kl_\gamma - \mu\frac{\pi}{2} - m\frac{\pi}{2} - \frac{\pi}{4} = kl_\gamma - m\frac{\pi}{2} - \frac{3\pi}{4}, \tag{27}$$

which is the same for both components of the spinor wavefunction. For a scarring state to form about this FDO with counterclockwise orientation, $\Phi_+^{(m)}$ needs to be an integer multiple of 2π: $\Phi_+^{(m)} = 2n\pi$, or

$$k_n^+ = (n + \frac{m}{4} + \frac{3}{8}) \times \frac{2\pi}{l_\gamma}. \tag{28}$$

If the particle travels along the FDO reversely from B to A, the phase change of the motion direction due to the reflection at the boundary is $\Delta\theta = 3\pi/2$, as indicated in Fig. 5(b). Note that, when counting the angles, the direction needs to be fixed, e.g., counterclockwise, so that further complexities of the reflection coefficients can be avoided [13, 17]. The orbit connects back to B via the phase relation Eq. (23) as

$$\begin{aligned} \widetilde{\psi}_j^{(m)}\big|_B &= \begin{pmatrix} e^{im\frac{\pi}{2}} & 0 \\ 0 & e^{i(m+1)\frac{\pi}{2}} \end{pmatrix} M_s(\frac{3\pi}{2}) M_{l_\gamma,\mu} \psi_j^{(m)}\big|_B \\ &\equiv K_{\gamma^-} M_{l_\gamma,\mu} \psi_j^{(m)}\big|_B \\ &\equiv \exp(i\Phi_-^{(m)}) \psi_j^{(m)}\big|_B, \end{aligned}$$

where

$$K_{\gamma^-} = \begin{pmatrix} e^{im\frac{\pi}{2}} & 0 \\ 0 & e^{i(m+1)\frac{\pi}{2}} \end{pmatrix} M_s(\frac{3\pi}{2}) = e^{im\frac{\pi}{2}} \begin{pmatrix} e^{-i\frac{3\pi}{4}} & 0 \\ 0 & e^{i\frac{5\pi}{4}} \end{pmatrix} = e^{im\frac{\pi}{2}-i\frac{3\pi}{4}} \mathbb{1}_2,$$

and

$$\Phi_-^{(m)} = kl_\gamma - \mu\frac{\pi}{2} + m\frac{\pi}{2} - \frac{3\pi}{4} = kl_\gamma + m\frac{\pi}{2} - \frac{5\pi}{4}. \tag{29}$$

Note that $M_{l_\gamma,\mu}$ is the same for both forward and backward directions. Correspondingly, the quantization condition for a scarring state about this FDO with the same direction is $\Phi_-^{(m)} = 2n\pi$, or

$$k_n^- = (n - \frac{m}{4} + \frac{5}{8}) \times \frac{2\pi}{l_\gamma}. \tag{30}$$

Denoting $A^{(m)}_{\gamma^\pm}$ as the amplitude of the contribution to the length spectra from the states along the FDO $A-B-A$ (denoted by "+") and its reversed counterpart $B-A-B$ (denoted by "−") of orbital length l_γ, we have [2]

$$A^{(m)}_{\gamma^+} = e^{i\Delta\Phi} A^{(m)}_{\gamma^-}, \tag{31}$$

where $\Delta\Phi = \Phi^{(m)}_+ - \Phi^{(m)}_- = \frac{\pi}{2} - m\pi$. The height of the peak in the length spectrum at length l_γ is

$$|\rho_{\rm osc}(l_\gamma)|^2 = |1+e^{i\Delta\Phi}|^2 |A^{(m)}_{\gamma^-}|^2 = 2|A^{(m)}_{\gamma^-}|^2, \tag{32}$$

regardless of the values of m.

For a combination of different subspaces, e.g., m_1 and m_2, assume

$$A^{(m)}_{\gamma^\pm} = e^{i\Phi^{(m)}_\pm} A_0(l_\gamma), \tag{33}$$

and

$$\begin{aligned} |\rho^{(m_1,m_2)}_{\rm osc}(l_\gamma)|^2 &\sim |A^{(m_1)}_{\gamma^+} + A^{(m_1)}_{\gamma^-} + A^{(m_2)}_{\gamma^+} + A^{(m_2)}_{\gamma^-}|^2 \\ &\sim |e^{i\Phi^{(m_1)}_+} + e^{i\Phi^{(m_1)}_-} + e^{i\Phi^{(m_2)}_+} + e^{i\Phi^{(m_2)}_-}|^2 |A_0(l_\gamma)|^2. \end{aligned} \tag{34}$$

Substituting Eqs. (27) and (29), and searching for all combinations of (m_1, m_2), we find that, for $(m_1, m_2) = (0,1)$ and (2,3), the following holds:

$$|\rho^{(m_1,m_2)}_{\rm osc}(l_\gamma)|^2 \sim 8|A_0(l_\gamma)|^2 \sim 4|\rho^{(m)}_{\rm osc}(l_\gamma)|^2. \tag{35}$$

For all other combinations, we have

$$|\rho^{(m_1,m_2)}_{\rm osc}(l_\gamma)|^2 \sim 0. \tag{36}$$

Equations (35) and (36) are consistent with the length spectra peaks for FDOs (1-3) in Fig. 4(b). In particular, the peaks in the length spectra for the square FDOs vanish when the symmetric subspaces (0,2) or (0,3) are combined. Heuristically, we check the phase interference in their mixtures

$$\begin{aligned} |\rho^{(0,2)}_{\rm osc}(l)|^2 &\sim |A^{(0)}_{\gamma^+} + A^{(0)}_{\gamma^-} + A^{(2)}_{\gamma^+} + A^{(2)}_{\gamma^-}|^2 \\ &\sim |e^{i\frac{\pi}{2}} + 1 + e^{-i\frac{\pi}{2}} + e^{i\pi}|^2 |A^{(0)}_{\gamma^-}|^2 = 0. \end{aligned} \tag{37}$$

$$\begin{aligned} |\rho^{(0,3)}_{\rm osc}(l)|^2 &\sim |A^{(0)}_{\gamma^+} + A^{(0)}_{\gamma^-} + A^{(3)}_{\gamma^+} + A^{(3)}_{\gamma^-}|^2 \\ &\sim |e^{i\frac{\pi}{2}} + 1 + e^{i\pi} + e^{-i\frac{\pi}{2}}|^2 |A^{(0)}_{\gamma^-}|^2 = 0. \end{aligned} \tag{38}$$

Similarly, $|\rho^{(1,2)}_{\rm osc}(l)|^2$ and $|\rho^{(1,3)}_{\rm osc}(l)|^2$ are also found to be zero.

3.2. Bouncing ball orbits (4-6)

For the bouncing ball orbits (4-6) that pass through the center of the billiard, the corresponding scarring states have the structure of a cross, because the solution is invariant under a $\pi/2$ rotation. To analyze the phase of such an orbit, we modify

the orbit to generate an infinitely narrow rectangle, as indicated in Fig. 5(b), where the two boundary points A and B are infinitesimally close to each other but on the two sides of the center. The two points A and B are related by a rotation of $\Delta\theta = \pi$, leading to the phase relation:

$$\psi_j^{(m)}\big|_A = \begin{pmatrix} e^{-im\pi} & 0 \\ 0 & e^{-i(m+1)\pi} \end{pmatrix} \psi_j^{(m)}\big|_B. \tag{39}$$

Thus after a rotation from A to B, one spinor component changes its sign.

Consider a spinor particle that travels from A to B following the FDOs and teleports back to A because of the phase relation Eq. (39). We have

$$\widetilde{\psi}_j^{(m)}\Big|_A = \begin{pmatrix} e^{-im\pi} & 0 \\ 0 & e^{-i(m+1)\pi} \end{pmatrix} M_s(\pi) M_{l_\gamma,\mu} \psi_j^{(m)}\Big|_A = \exp(i\Phi_+^{(m)}) \psi_j^{(m)}\Big|_A, \tag{40}$$

where M_s and $M_{l_\gamma,\mu}$ are given by Eqs. (25) and (26), respectively. Therefore

$$\Phi_+^{(m)} = k l_\gamma - m\pi - \pi. \tag{41}$$

The resulting quantization condition for the scarring states around this FDO is

$$k_n^+ = (n + \frac{m}{2} + \frac{1}{2}) \times \frac{2\pi}{l_\gamma}. \tag{42}$$

Similarly, through

$$\widetilde{\psi}_j^{(m)}\Big|_B = \exp(i\Phi_-^{(m)})\, \psi_j^{(m)}\Big|_B,$$

we have

$$\Phi_-^{(m)} = k l_\gamma + m\pi - \pi \tag{43}$$

for the reversed direction. The corresponding quantization condition is

$$k_n^- = (n - \frac{m}{2} + \frac{1}{2}) \times \frac{2\pi}{l_\gamma}. \tag{44}$$

For the peaks in the length spectra for a subspace m, we have $\Delta\Phi = -2m\pi = 0 \bmod 2\pi$, because the FDOs are indistinguishable between the forward and backward directions. The height of the peak in the length spectrum at length l_γ is

$$|\rho_{\rm osc}(l_\gamma)|^2 = |1 + e^{i\Delta\Phi}|^2 |A_{\gamma^-}^{(m)}|^2 = 4|A_{\gamma^-}^{(m)}|^2, \tag{45}$$

which is independent to m. That is, the heights of the length spectra peaks for the orbits (1-3) should be the same for different m subspaces.

When the two symmetric subspaces m_1 and m_2 are combined, Eq. (34) indicates that a search over all possible combinations yields

$$|\rho_{\rm osc}^{(m_1,m_2)}(l_\gamma)|^2 \sim 16|A_0(l_\gamma)|^2 \sim 4|\rho_{\rm osc}^{(m)}(l_\gamma)|^2$$

for $(m_1, m_2) = (0, 2)$ and (1,3). For all other combinations, we have

$$|\rho_{\rm osc}^{(m_1,m_2)}(l_\gamma)|^2 \sim 0.$$

Again, this is consistent with the length spectra peaks for the FDOs (4-6) in Fig. 4(b).

3.3. The bouncing ball orbit (7) within a fundamental domain

Orbit (7) is a bouncing ball orbit residing completely inside a fundamental domain without intersecting any symmetry line, as shown in Fig. 4(c). The four-fold rotational symmetry does not impose any constraint on this orbit, so the quantization condition is the same as in a conventional billiard, i.e., the total phase accumulation after a complete cycle around the orbit is an integer multiple of 2π. As a result, the peak at length l_γ of this orbit appears in any symmetric subspace as well as in any combination of a pair of symmetric subspaces, with the height four times of that of a single symmetric subspace. The peak for this orbit also appears in the length spectra when all the symmetric subspaces are combined, with the height 16 times of that for a single symmetric subspace.

3.4. The missing parallelogram orbit (8)

The parallelogram orbit has half length in the fundamental domain, but it does not emerge at the position (8) in the length spectra in Fig. 4. To understand this behavior, we focus on the traveling path of the FDO $A-A'-B'-B-A$ in the fundamental domain and its reversed counterpart $B-B'-A'-A-B$, as shown in Figs. 5(d) and 5(e), respectively. For the forward orbit, the requirement that the wavefunction must be a single value function yields

$$\begin{aligned}\widetilde{\psi}_j^{(m)}\big|_A = &\begin{pmatrix} e^{-im\frac{\pi}{2}} & 0 \\ 0 & e^{-i(m+1)\frac{\pi}{2}} \end{pmatrix} \times M_s(\Delta\theta_{BB'}) M_{l_\gamma,\mu}(l_{BB'}) \\ &\times \begin{pmatrix} e^{-im\frac{\pi}{2}} & 0 \\ 0 & e^{-i(m+1)\frac{\pi}{2}} \end{pmatrix} \times M_s(\Delta\theta_{A'A}) M_{l_\gamma,\mu}(l_{A'A}) \psi_j^{(m)}\big|_A = \exp(i\Phi_+^{(m)})\psi_j^{(m)}\big|_A,\end{aligned}$$

where $l_{A'A}$ and $l_{BB'}$ are the length of the orbit from A to A' and from B' to B, respectively, $\Delta\theta_{AA'} = \Delta\theta_{B'B} = \pi/2$ denote the angle change at the two reflection points, and

$$\Phi_+^{(m)} = kl_\gamma - m\pi - \frac{3\pi}{2} \tag{46}$$

modulo 2π, where $l_\gamma = l_{AA'} + l_{B'B}$ is the total length of the FDO.

For the backward path $B-B'-A'-A-B$, we have

$$\begin{aligned}\widetilde{\psi}_j^{(m)}\big|_B = &\begin{pmatrix} e^{im\frac{\pi}{2}} & 0 \\ 0 & e^{i(m+1)\frac{\pi}{2}} \end{pmatrix} \times M_s(\Delta\theta_{AA'}) M_{l_\gamma,\mu}(l_{AA'}) \\ &\times \begin{pmatrix} e^{im\frac{\pi}{2}} & 0 \\ 0 & e^{i(m+1)\frac{\pi}{2}} \end{pmatrix} \times M_s(\Delta\theta_{B'B}) M_{l_\gamma,\mu}(l_{B'B}) \psi_j^{(m)}\big|_B = \exp(i\Phi_-^{(m)})\psi_j^{(m)}\big|_B,\end{aligned}$$

where $\Delta\theta_{B'B} = \Delta\theta_{AA'} = 3\pi/2$, and

$$\Phi_-^{(m)} = kl_\gamma + m\pi - \frac{\pi}{2} \tag{47}$$

modulo 2π. The phase difference between the forward and backward FDO is $\Delta\Phi = \Phi_+^{(m)} - \Phi_-^{(m)} = \pi \bmod 2\pi$, regardless of the m values. Its contribution to the length spectra is

$$\rho_{\rm osc}(l_\gamma)^2 = |1 + e^{i\Delta\Phi}|^2 |A_{\gamma^-}^{(m)}|^2 = 0, \tag{48}$$

explaining the disappearance of the length spectra peaks for the parallelogram FDO. Since the peak is absent in each subspace, it does not appear in any combination of different subspaces.

4. Quantization and statistics of scarring states in a symmetric subspace

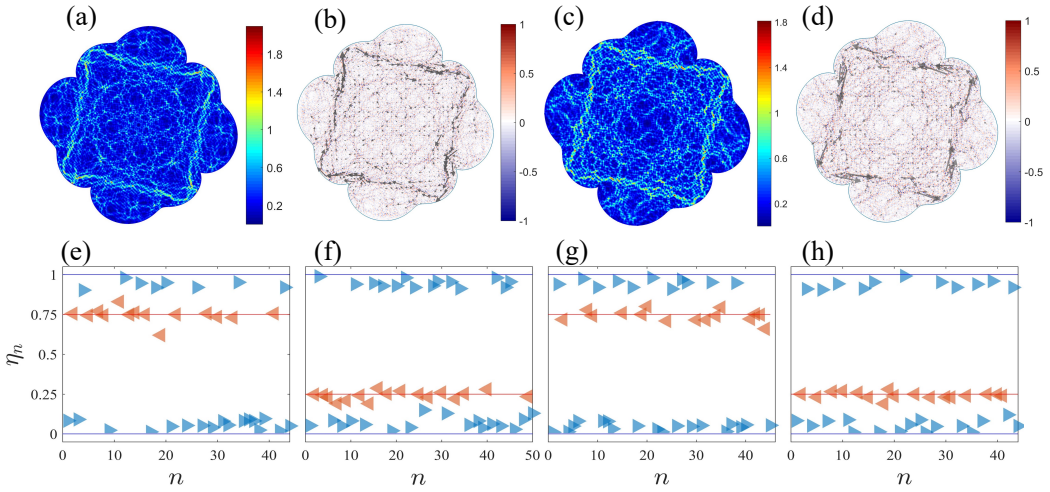

Figure 6. Examples of square scars and η_n statistics for the scarring wavefunctions. (a) The intensity distribution of the 2034th wavefunction in the subspace $H^{(3)}$, (b) the corresponding local current $\boldsymbol{j}(\boldsymbol{r})$ (arrows, clockwise) and $\langle\sigma_z\rangle$ (color scale). (c) The intensity distribution of the 2535th wavefunction in $H^{(3)}$, (d) its local current $\boldsymbol{j}(\boldsymbol{r})$ (arrows, counterclockwise) and $\langle\sigma_z\rangle$ (color scale). (e-h) The η_n statistics for the scarring wavefunctions around the square orbit in the subspaces $H^{(m)}$ for $m = 0$, 1, 2 and 3, respectively. The left and right triangles indicate the states with counterclockwise and clockwise currents, respectively. The horizontal solid lines indicate the predicted values.

Since the bouncing ball orbits (4-7) are identical for the forward and backward directions and the scarring states around the FDO (8) are too few to generate reliable statistics, we focus on the square type of orbits, e.g., the FDO (2). Figures 6(a)-6(d) plot the spinor wavefunction intensity $|\psi_j^{(m)}|^2 = |\psi_{j,1}^{(m)}|^2 + |\psi_{j,2}^{(m)}|^2$ for $m = 3$ and $j = 2034$ and 2535, and their corresponding local clockwise or counterclockwise currents as determined by Eq. (3). Note that, since $\hat{\boldsymbol{j}} = v_F\hat{\boldsymbol{\sigma}}$ and v_F is a constant, the local current $\boldsymbol{j}(\boldsymbol{r})$ also reveals the expectation value of $\hat{\boldsymbol{\sigma}}$. In addition, we have $\langle\sigma_z\rangle = \psi^\dagger\sigma_z\psi = |\psi_1|^2 - |\psi_2|^2$, which complements the intensity. We plot $\langle\sigma_z\rangle$ in Figs. 6(a) and 6(d) on different color scales. It can be seen that $\langle\sigma_z\rangle$ is prominent along the square periodic orbits and oscillates on the wavelength scale because the two components are related by Eq. (2).

According to Eq. (27), for a scarring state to form about this FDO with the forward direction (counterclockwise orientation), the phase $\Phi_+^{(m)}$ needs to be an integer multiple of 2π to ensure that the wavefunctions are single valued, i.e., $\Phi_+^{(m)} = 2n\pi$, which leads to Eq. (28) for k_n^+. If the particle travels along the FDO reversely from B to A, Eq. (29) stipulates that the quantization condition for a scarring state around this FDO with the same direction is $\Phi_-^{(m)} = 2n\pi$, leading to Eq. (30) for k_n^-. Consequently, for a given subspace m, two sets of the scarring states with opposite directions arise. Neglecting the integer part (modulo of 2π), the phase difference between the counterclockwise and clockwise flow states is $(m/2 - 1/4)$ in units of 2π, so for $m = 0$ and 2, it is $-1/4$, and $3/4$ mod 1 (2π), while for $m = 1$ and 3, the difference is $1/4$ (2π). This can be characterised by the semiclassical η statistics [16]. Specifically, after a set of scars with wavenumbers k_n being identified, a particular one can be chosen with its wave number set as the reference point k_0. The η quantity can be calculated as

$$\eta = \frac{|k_n - k_0|}{\Delta k} - [\frac{|k_n - k_0|}{\Delta k}], \tag{49}$$

where $\Delta k = 2\pi/l_\gamma$, l_γ is the length of the FDOs, and $[x]$ returns the maximum integer equal to or less than x. We have identified about 45 scarring states in each subspace. In Fig. 6(e-h), the reference point k_0 is chosen to be associated with a scarring state with the clockwise orientation (right triangles). Then all the scarring states with the same orientation takes on η values about either zero or one, while those with opposite orientations (left triangles) are about $3/4$ for $m = 0$ and 2, and $1/4$ for $m = 1$ and 3. The numerically observed η statistics (data points) agree well with the results from our phase analysis (horizontal lines).

5. Discussion

The main accomplishments of this work are as follows. We have investigated the length spectra and the quantum scarring states in a 2D massless chaotic Dirac billiard with the four-fold rotational symmetry. Since the Hamiltonian commutes with the rotation operator of $\pi/2$, the Hamiltonian matrix can be reorganized in a blocked form with four subspaces $H^{(m)}$ ($m = 0$, 1, 2, and 3), where the relativistic quantum properties of the spinor wavefunction in each subspace are analyzed using a billiard consisting of only one fundamental domain. In this "effective" billiard system, in addition to the infinite-mass boundary condition for the original billiard, a connection condition on the symmetry lines imposed by requiring the same physical properties under the symmetry operation is necessary. For each subspace, we have analyzed the accumulated spin-induced phases along the FDOs and found that, due to the interference along a forward (counterclockwise) direction of the FDO and that for the backward direction, the peaks of the length spectra can be either enhanced or destroyed. For various combined subspaces, the interference can be more complicated.

It has been known previously that, if there is time-reversal symmetry breaking in the system, e.g., in a Dirac billiard with infinite-mass confinement or in a Schrödinger

billiard subject to a singular Aharonov-Bohm magnetic flux, a non-2π phase can exist between the wavefunctions in the two opposite directions, which may lead to destructive interference in their contribution to the peaks in the length spectra, as observed in Dirac billiards [17, 50] and in nonrelativistic quantum billiards with a geometric symmetry [48]. Our present work has elucidated the role played by the FDOs in the sophisticated relativistic quantum interference process. In particular, comparing with the results in nonrelativistic quantum billiards with the four-fold symmetry [48], the accumulated phase in the Dirac billiard with the same symmetry is quite distinct, leading to disparate interference patterns and drastically distinctive length spectral peaks. For example, in the length spectra of a single subspace, FDO (8) has the most prominent peak in the nonrelativistic case, but it disappears completely in the relativistic Dirac billiard case [Fig. 4(a)]. Characteristically distinctive behavior also exists for other orbits. In addition, our phase-based theoretical analysis yields results on the length spectra that agree well with the numerical data. We have also demonstrated that, from the exact formula of the accumulated phase along the FDOs, the quantization conditions underlying the scarring states in each symmetric subspace can be derived. These conditions allow us to determine the relative phase between the forward and backward states, as characterized by the local current flow, which agrees with the statistics for the scarring states within each symmetry class. Taken together, our work is another concrete proof that the powerful principle of geometric phase analysis pioneered by Sir Michael Berry can be exploited to understand intriguing physical phenomena arising from the interplay among chaos, symmetry, and relativistic quantum mechanics.

Acknowledgments

The work at Lanzhou University was supported by NSFC under Grant Nos. 12175090, 11775101, and 12047501, and by the 111 Project under Grant No. B20063. The work at Arizona State University was supported by the Air Force of Scientific Research through Grant No. FA9550-21-1-0186.

References

[1] Berry M V 1989 *Proc. R. Soc. London Series A Math. Phys. Eng. Sci.* **423** 219–231
[2] Stöckmann H J 2006 *Quantum Chaos: An Introduction* (New York: Cambridge University Press)
[3] Haake F 2010 *Quantum Signatures of Chaos* 3rd ed Springer series in synergetics (Berlin: Springer-Verlag)
[4] Blümel R and Smilansky U 1989 *Physica D* **36** 111–136
[5] Blümel R and Smilansky U 1989 *Phys. Scrip.* **40** 386–393
[6] Kottos T and Smilansky U 1997 *Phys. Rev. Lett.* **79**(24) 4794–4797
[7] Primack H and Smilansky U 1998 *J. Phys. A. Math. Gen.* **31** 6253–6277
[8] Cohen D, Primack H and Smilansky U 1998 *Ann. Phys.* **264** 108–170
[9] Smilansky U 2000 *J. Phys. A. Math. Gen.* **33** 2299–2312
[10] Kottos T and Smilansky U 2000 *Phys. Rev. Lett.* **85**(5) 968–971
[11] Primack H and Smilansky U 2000 *Phys. Rep.* **327** 1–107
[12] Gnutzmann S and Smilansky U 2006 *Adv. Phys.* **55** 527–625

[13] Berry M V and Mondragon R J 1987 *Proc. R. Soc. London Series A Math. Phys. Eng. Sci.* **412** 53–74
[14] Lai Y C, Xu H Y, Huang L and Grebogi C 2018 *Chaos* **28** 052101
[15] Huang L, Xu H Y, Grebogi C and Lai Y C 2018 *Phys. Rep.* **753** 1–128
[16] Xu H, Huang L, Lai Y C and Grebogi C 2013 *Phys. Rev. Letts.* **110** 064102
[17] Wang C Z, Huang L and Chang K 2017 *New J. Phys.* **19** 013018
[18] McDonald S W and Kaufman A N 1979 *Phys. Rev. Lett.* **42**(18) 1189–1191
[19] Heller E J 1984 *Phys. Rev. Letts.* **53** 1515–1518
[20] Song M Y, Li Z Y, Xu H Y, Huang L and Lai Y C 2019 *Phys. Rev. Research* **1** 033008
[21] Neto A H C and Novoselov K 2011 *Mater. Exp.* **1** 10–17
[22] Ajayan P, Kim P and Banerjee K 2016 *Phys. Today* **69** 38–44
[23] Novoselov K S, Geim A K, Morozov S V, Jiang D, Zhang Y, Dubonos S V, Grigorieva I V and Firsov A A 2004 *Science* **306** 666–669
[24] Novoselov K S, Geim A K, Morozov S V, Jiang D, Katsnelson M I, Grigorieva I V, Dubonos S V and Firsov A A 2005 *Nature* **438** 197–200
[25] Zhang Y B, Tan Y W, Stormer H L and Kim P 2005 *Nature* **438** 201–204
[26] Huang L and Lai Y C 2020 *Commun. Theor. Phys.* **72** 047601
[27] Cvitanović P and Eckhardt B 1993 *Nonlinearity* **6** 277–311
[28] Leyvraz F, Schmitd C and Seligman T H 1996 *J. Phys. A Math. Gen.* **29** L575–L580
[29] Dembowski C, Gräf H D, Heine A, Rehfeld H, Richter A and Schmit C 2000 *Phys. Rev. E* **62**(4) R4516–R4519
[30] Schafer R, Barth M, Leyvraz F, Muller M, Seligman T H and Stockmann H J 2002 *Phys. Rev. E* **66** 016202
[31] Dembowski C, Dietz B, Gräf H D, Heine A, Leyvraz F, Miski-Oglu M, Richter A and Seligman T H 2003 *Phys. Rev. Lett.* **90** 014102
[32] Mehta M L 2004 *Random Matrices* vol 142 (Academic press)
[33] Bohigas O, Giannoni M J and Schmit C 1984 *Phys. Rev. Lett.* **52** 1–4
[34] Andreev A V, Agam O, Simons B D and Altshuler B L 1996 *Phys. Rev. Lett.* **76** 3947–3950
[35] Guhr T, Groeling A M and Weidenmüller H A 1998 *Phys. Rep.-Rev. Sec. Phys. Lett.* **299** 189–425
[36] Mehta M L and Wigner E P 2001 Review of 'Random Matrices and the Statistical Theory of Energy Levels' *Historical and Biographical Reflections and Syntheses* ed Mehra J (Berlin, Heidelberg: Springer Berlin Heidelberg) pp 506–507
[37] Gu Y 1996 *Quantum Chaos* (Shanghai Scientific and Technological Education Publishing House)
[38] Casati G and Chirikov B 2006 *Quantum Chaos: Between Order and Disorder* (Cambridge University Press)
[39] Berry M V and Tabor M 1977 *Proc. Royal Soc. A* **356** 375–394
[40] Stöckmann H J and Stein J 1990 *Phys. Rev. Lett.* **64**(19) 2215–2218
[41] Sridhar S 1991 *Phys. Rev. Lett.* **67**(7) 785–788
[42] Gräf H D, Harney H L, Lengeler H, Lewenkopf C H, Rangacharyulu C, Richter A, Schardt P and Weidenmüller H A 1992 *Phys. Rev. Lett.* **69**(9) 1296–1299
[43] So P, Anlage S M, Ott E and Oerter R N 1995 *Phys. Rev. Lett.* **74**(14) 2662–2665
[44] Robbins J M 1989 *Phys. Rev. A* **40** 2128–2136
[45] Lauritzen B 1991 *Phys. Rev. A* **43** 603
[46] Seligman T H and Weidenmüller H A 1994 *J. Phys. A-Math. Theor.* **27** 7915–7923
[47] Keating J P and Robbins J 1997 *J. Phys. A-Math. Theor.* **30** L177
[48] Li Z Y and Huang L 2020 *Phys. Rev. E* **101**(6) 062201
[49] Zhang W and Dietz B 2021 *Phys. Rev. B* **104**(6) 064310
[50] Song M Y, Li Z Y, Xu H Y, Huang L and Lai Y C 2019 *Phys. Rev. Research* **1**(3) 033008
[51] Bolte J and Keppeler S 1998 *Phys. Rev. Lett.* **81**(10) 1987–1991
[52] Bolte J and Keppeler S 1999 *Ann. Phys.* **274** 125–162
[53] Keppeler S 2003 *Ann. Phys.* **304** 40–71

[54] Wurm J, Richter K and Adagideli I 2011 *Phys. Rev. B* **84**(20) 205421
[55] Vogl M, Pankratov O and Shallcross S 2017 *Phys. Rev. B* **96**(3) 035442